Investigating the effect of Zn doping on physical properties of nanostructured Sb$_2$S$_3$ thin films by dip-coating technique

F. Chharganeh Kalangestani[1] · F. E. Ghodsi[1] · Z. Bazhan[1]

Abstract

In this research, the effect of zinc doping on physical properties of Sb$_2$S$_3$ thin films grown by the sol–gel dip-coating method, on the glass substrates was investigated. XRD patterns indicated that the Zn$_x$(Sb$_2$S$_3$)$_{1-x}$ ($x=0.02, 0.05, 0.07, 0.1$) thin films have orthorhombic crystalline structure while the intensity of the peaks decreased with increasing Zn contamination. The FESEM images demonstrated that the grain size decreased with increasing Zn concentration. The porosity of the samples changed by different values of Zn. The optical transmission spectra exhibited a shift in the absorption edge for various zinc concentrations. The refractive index of sample with $x=0.02$ has the highest value among all samples. In addition, the band gap of thin films is about 2.4–3.6 eV. The PL spectra showed the doped sample with the x value of 0.02 which has the highest visible emission. Also, the contact angle measurements showed that the surface of the films were hydrophilic.

Keywords Sb$_2$S$_3$ thin films · Nanostructured · Dip-coating · Sol–gel

1 Introduction

Semiconductor nanostructures have received a lot of attention over the last few years due to new electrical and optical properties. These new optical properties have performance in the many potential applications such as solar energy conversion, optical devices, chemical or biological sensors and photocatalysis. Among all semiconductors, chalcogenides material such as M$_2$X$_3$ (M = As, Sb, Bi; X = S, Se, or Te) have great importance in the field of nanoscale due to their widespread use in optoelectronic devices including photovoltaics. Among the available chalcogenides, antimony sulfide is a V–VI group semiconductor and contains many minerals in the Earth's crust and in nature [1, 2]. Antimony is a silvery white, brittle, crystalline solid that transmits poor electricity and heat. Antimony is rarely found in nature due to its strong bond with sulfur and metals such as copper, lead and silver as a pure metal [3, 4]. Due to its high absorption coefficient (1.8×10^5 cm^{-1} at 450 nm), low cost extraction and low toxicity, antimony sulfide films have attracted much attention in the photoelectric fields. In addition,

Sb$_2$S$_3$-based solar cells have good photovoltaic performance in poor lighting conditions. Therefore, research on antimony sulfide solar cells for the next generation of photovoltaics is very valuable [5]. Various techniques, such as sputtering [6], chemical bath deposition [7], aerosol-assisted chemical vapor deposition (AACVD) [8], thermal evaporation [9], pulse electrodeposition [10], physical vapor deposition [11] and sol–gel spin-coating method [12], have been used to deposit Sb$_2$S$_3$ nanostructured thin films. The results indicate that the properties of Sb$_x$S$_{1+x}$ thin films strongly depend on the preparation conditions and growth methods. Compared to other processes, the sol–gel process proved to be more effective to prepare semiconductor nanostructures especially thin films on the glass substrates at low temperatures. Gil et al. [12] have reported a simple spin-coating process for depositing the Sb$_2$S$_3$ thin film with various process conditions such as the composition and concentration of the precursor solutions, the number of spin coatings, and the spin speed. The surface morphology of the films showed that when the molar ratio of SbCl$_3$:Tu = 1:1, it was achieved a uniform Sb$_2$S$_3$ thin film. With the increase of thiourea, several separated Sb$_2$S$_3$ dense grains were formed, which it was impossible to make a uniform Sb$_2$S$_3$ thin film. Also with the increase in the number of spin-coating cycles (more than three cycle), uniform and continuous Sb$_2$S$_3$ thin films were successfully formed on the substrate. They

✉ F. E. Ghodsi
feghodsi@guilan.ac.ir

1 Department of Physics, Faculty of Science, University of Guilan, Namjoo Avenue, P.O. Box 413351914, Rasht, Iran

were obtained uniform and high quality Sb_2S_3 thin films by optimizing the process conditions. Nwofe et al. [13] used the chemical bath deposition method to deposit Zn-doped Sb_2S_3 thin films. The compositional characterization by the Rutherford Backscattering techniques exhibited that the film thicknesses constantly increased with an increase in the Zn doping concentration from 0.25 up to 1.00 M. To improve the power conversion efficiency of Sb_2S_3-based solar cells, Tang et al. [14] prepared Zn-doped Sb_2S_3 thin films by the spin-coating method. They showed that doping of Zn ions slightly reduces the band gap and enhances the crystallinity. Also, much high doping concentration would increasingly cause generated pinholes in the film, which induces serious recombination in the device. The photovoltaic parameters, short-circuit current density, open-circuit voltage, and the fill factor of the device based on the Sb_2S_3 film are all considerably enhanced, boosting the final power conversion efficiency from 5.15 to 6.35%.

In the present research, for the first time, Zn-doped Sb_2S_3 thin films were deposited on glass substrates by sol–gel dip-coating method. To the best of our knowledge, so far, there has been no report concerning to the effects of Zn doping on the physical properties including wettability properties of sol–gel derived Sb_2S_3 thin films. Also, doping concentration was taken as the experimental parameter to study the alterations in structural, morphological and optical properties.

2 Experimental

2.1 Preparation solutions

In this study, the following procedure was adopted for the preparation of sol. Antimony trichloride ($SbCl_3$) and thiourea [$SC(NH_2)_2$] were used as precursors. For solution with molarity 0.5 mol/L, first, 1.141 g of antimony trichloride was dissolved in 10 mL of 2-methoxyethanol solvent and stirred for 30 min at room temperature with a magnetic stirrer at 60 rpm. Then 0.381 g of thiourea was added to the colorless transparent solution and stirred at room temperature at 60 rpm for 20 min. to give a homogeneous transparent pale yellow solution. At the doping stage, zinc acetate dihydrate was added to the solution at concentrations of 2%, 5%, 7% and 10% and stirred at room temperature for 60 min at 60 rpm. Finally, 0.1 mL of diethanolamine stabilizer was poured into the solution and stirred until complete solubilization to obtain clear solubility at 60 rpm without heating.

2.2 Film deposition

After 6 days of sol preparation, the deposition phase of antimony sulfide thin films began. The Zn-doped Sb_2S_3 thin films were prepared by the sol–gel dip-coating method. The Zn-doped Sb_2S_3 thin films were deposited on glass substrates using the dip-coating method. The withdrawal speed of the substrate from the coating was 105 mm/min. Then, the films were dried at 140 °C to evaporate the solvent and remove organic residuals. This coating and drying procedure was repeated several times to produce layers of sol on the substrate. Then, the samples were annealed in a furnace at 350 °C for 1 h in N_2 atmosphere for crystallization. Upon annealing, the thin film was ready to be analyzed for its characteristics.

The infrared transmission spectrum of powder sample was recorded using Fourier transformed infrared (FTIR) spectrophotometer (Alpha-Braker) to identify the chemical structure. The structural investigations were performed with a Philips PW-1840 diffractometer using CuKα radiation ($\lambda_{CuK\alpha} = 0.15406$ nm). The surface morphology and stoichiometry of the specimens was investigated using field emission scanning electron microscopy (FESEM) and energy dispersive X-ray (EDX) analysis MIRA3 TESCAN-XMU model. The transmission spectra of films were investigated with Varian Cary100 UV–Visible spectrophotometer. The optical constants (refractive index and extinction coefficient) of the films were calculated from the experimental spectral transmittance by Pointwise Unconstrained Minimization Approach (PUMA) method. The photoluminescence spectra of thin films were investigated by Perkin Elmer (LS 55) Fluorescence spectrometer and the wettability of films were investigated using water contact angle measurement by VEHO USB Microscope 400× camera.

3 Results and discussion

3.1 Structural properties

Figure 1 shows the X-ray diffraction patterns of the undoped and zinc-doped antimony sulfide samples. The patterns show that all samples have a polycrystalline structure and the intensity of the peaks decreases by adding zinc dopant. The secondary phase is not created by the addition of Zn, which indicates that there is no change in the Sb_2S_3 structure. The intensity of the peaks increases with the increasing concentration of zinc dopant up to 5%. However, with re-increasing the doping concentration, the intensity of the peaks decreases, which can be due to the high replacement of Zn atoms in the Sb_2S_3 lattice [15]. All defined peaks were matched with (JCPDS Card No.: 42-1393), confirming the orthorhombic phase for Sb_2S_3 in all samples [16–18]. In these patterns, three intensive peak around $2\theta = 25.07°$, 29.32° and 32.47° can be seen, which have apparently preferred orientation along (310), (211) and (221) directions, respectively. The average crystallite size (D) and strain of

Fig. 1 **a** X-ray diffraction patterns of the undoped and zinc-doped antimony sulfide samples. **b** The magnified XRD patterns of (310) plane of the samples
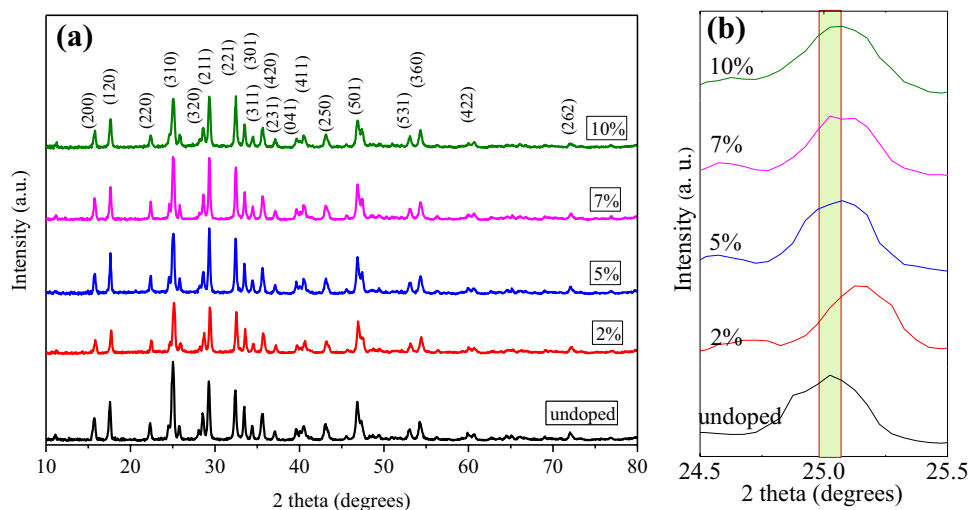
samples was calculated using the Williamson-Hall methods [19]:

$$\beta \mathrm{Cos}\theta = \frac{K\lambda}{D} + 4\varepsilon \mathrm{Sin}\theta \qquad (1)$$

where D is the crystallite size, K is a constant equal to 0.94, λ is the wavelength of the radiation (1.54056 Å for CuKα radiation), ε is the strain, β is full width at half maximum (FWHM) and θ is the Bragg diffraction angle. Also, the direct lattice volume and lattice constants (a, b and c) for the samples have been refined using Rietveld refinement method [20]. The calculated results average crystallite size and lattice parameters are reported in Table 1. The experimental, calculated and the difference XRD patterns are shown in Fig. 2. As it can be seen, there is a good agreement between the experimental and calculated patterns.

3.2 FTIR study

Figure 3 shows the Fourier transform infrared spectra of $Zn_x(Sb_2S_3)_{1-x}$ which confirms the formation of antimony sulfide bonds. In FTIR analysis, the bonds observed in the range of 2500–4000 cm⁻¹ are related of the O–H bond stretching vibration, which indicates the presence of water in the compound [21]. The peaks appearing in the range of 612, 742, and 1639 cm⁻¹ can be attributed to the Sb-S symmetric

stretching vibration. The absorption bands observed around 1072 and 1124 cm⁻¹ related to C–OH bond or charge delocalization [22, 23]. The peak at ~1278 cm⁻¹ is attributed to S–C bond [24]. The absorption peak at 1383 cm⁻¹ corresponds to metal-sulfide bond [23]. The peak appearing around 1463 cm⁻¹ is assigned to the C–H bond flexural vibration [25]. The peak at ~1729 cm⁻¹ is attributed to C=O stretching vibration [22]. Also, two peaks of 2870 and 3510 cm⁻¹ were observed in the transmission spectra of sample with the x value of 0.1, which may be related to Sb–Zn–O bonding [13]. The changes observed in the intensity, shape and position of the peaks are due to the interaction between the Zn and Sb₂S₃ particles.

3.3 Morphological properties

The FESEM images of Sb₂S₃ thin films with different zinc concentrations are shown in Fig. 4. FESEM images of thin films show that Sb₂S₃ nanostructure surface consists of large spherical grains, which the grains average diameter is of 70 nm. Some parameters such as the temperature difference between the film and the substrate, the pH-dependent ionic velocity and the deposition time, the temperature, and the type of the used substrates (amorphous or crystalline) affect the structure of the growing crystals [25]. By adding Zn dopant, the spacing of the grains increases. But with

Table 1 The structural parameters of the undoped and zinc-doped antimony sulfide samples

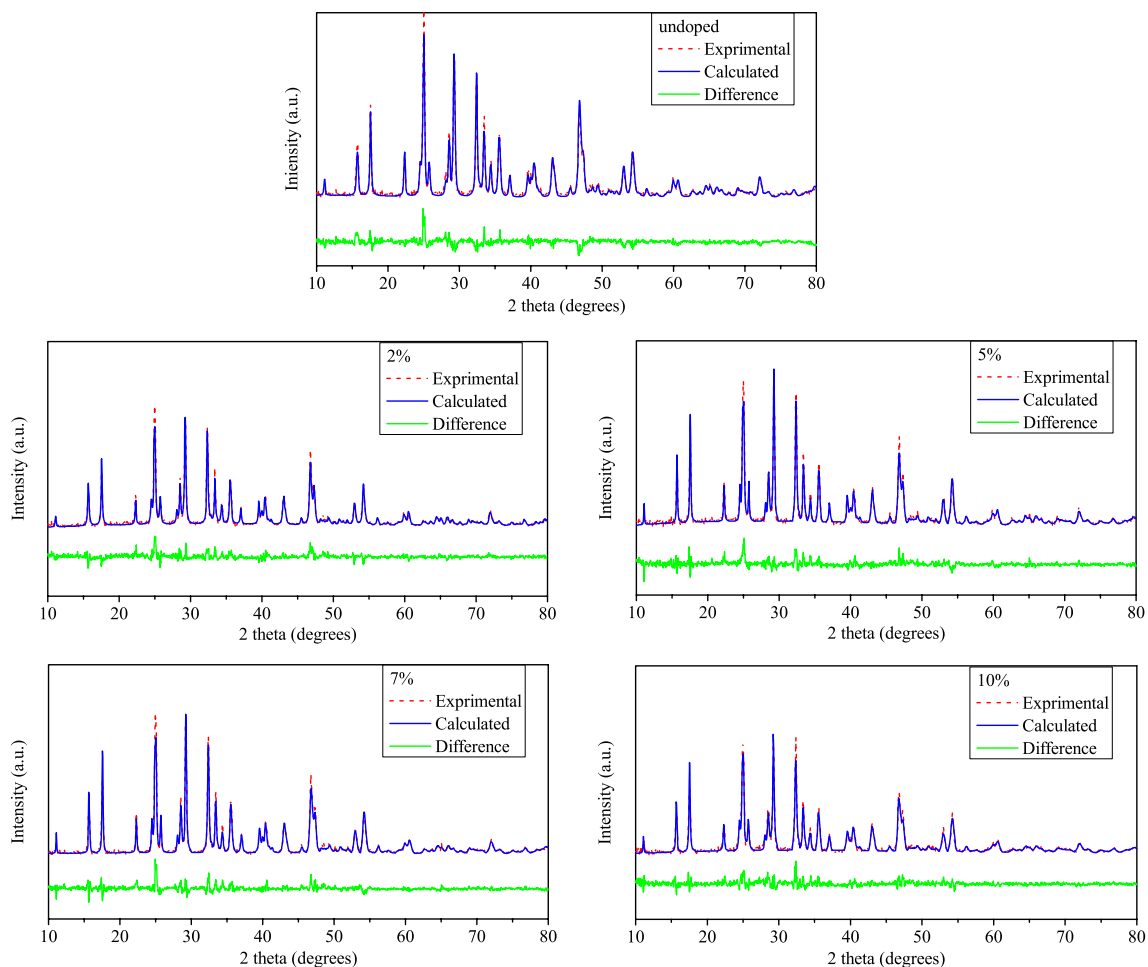| $Zn_x(Sb_2S_3)_{1-x}$ x (%)	D_{W-H} (nm)	strain	Lattice constants			Direct lattice volume (Å³)
			a (Å)	b (Å)	c (Å)	
0	35.63	0.00134	11.31	3.84	11.23	486.95
2	37.56	0.00124	11.26	3.83	11.20	482.49
5	42.78	0.00134	11.29	3.83	11.22	485.15
7	41.01	0.00135	11.28	3.83	11.21	484.31
10	35.36	0.00164	11.28	3.83	11.22	484.64

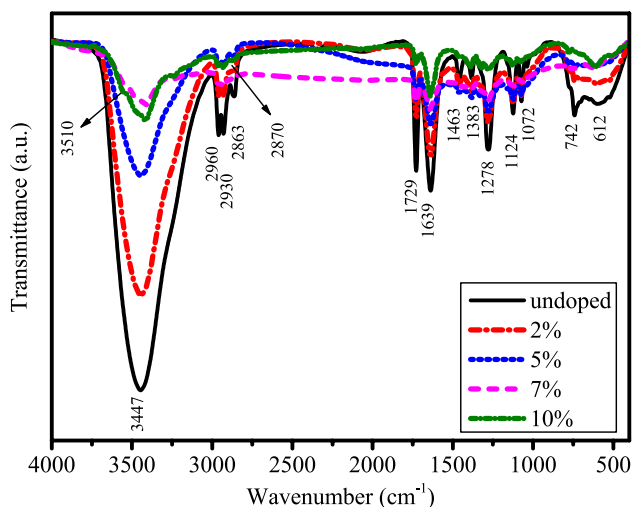**Fig. 2** The Rietveld refined XRD pattern of the undoped and zinc-doped antimony sulfide samples

Fig. 3 FTIR spectra of the typical prepared sol and thin films

increasing Zn concentration, the grain size again decreases, which reduces the porosity and more intertwined. According to XRD results, Zn doping does not produce a new phase in the films, however, it results to substitute the host atoms by Zn ions, which simultaneously changes the crystallite size and strain in the films [26]. The existence of the uneven distribution and the dense surface particles is one of the common characteristics reported in Sb_2S_3 thin films [15, 27]. X-ray energy scattering spectrum (EDS) was used to confirm the presence of zinc in the sample (Fig. 4f). The antimony, sulfide and zinc elements are well identified.

3.4 Wettability properties

The water contact angle for the $Zn_x(Sb_2S_3)_{1-x}$ thin films was measured to obtain the information about the wetting behavior of the prepared films surface. If water contact angle is less than 90°, the surface called hydrophilic and if it is larger than 90°, the surface called hydrophobic [28]. Water contact angle is given by Young's equation [29, 30]:

Fig. 4 FESEM images of $Zn_x(Sb_2S_3)_{1-x}$ thin films at 500 nm scale; **a** $x=0.00$, **b** $x=0.02$, **c** $x=0.05$, **d** $x=0.07$, **e** $x=0.1$, **f** X-ray energy scattering spectrum (EDS)
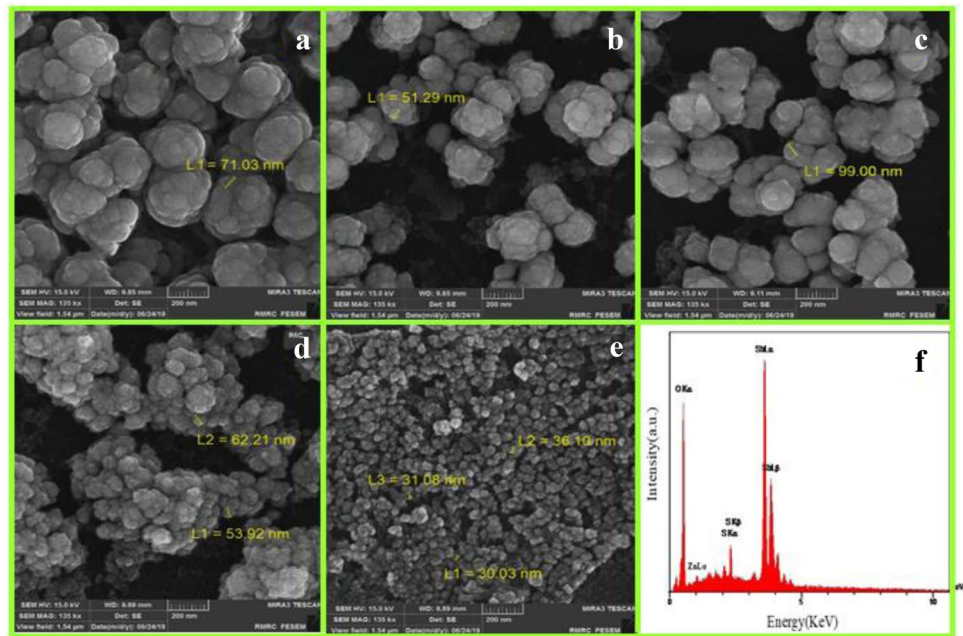
$$\text{Cos}\theta_Y = \frac{(\gamma_{SV} - \gamma_{SL})}{\gamma_{VL}} \qquad (2)$$

where γ_{SV}, γ_{SL}, and γ_{LV} display the interfacial free energy of solid–vapor, solid–liquid and liquid–vapor, respectively. Since surfaces are not completely smooth, usually, Wenzel modified the Young's equation by adding a coefficient [31]:

$$\text{Cos}\theta_W = r\text{Cos}\theta_Y \qquad (3)$$

where r is the roughness factor. If r is larger than one, the intrinsic wetting property of surface increases. If the air is surrounded by a droplet, the contact angle is calculated by the Cassie and Baxter equation [32]:

$$\text{Cos}\theta_{CB} = f\text{Cos}\theta_Y + (1-f) \qquad (4)$$

where f is the area fraction of droplet in contact with surface. The variation of water contact angle with amount of zinc for $Zn_x(Sb_2S_3)_{1-x}$ is shown in Fig. 5. The water droplet was dropped by the syringe on the film surface and the images of the drop were recorded using a camera. It has been observed that the angle of contact for Sb_2S_3 film with water is around 21°. This contact angle determines the hydrophilic nature of the Sb_2S_3 nanostructure, which this is conforming to the results obtained by other groups [33–35].

The small contact angle of the water increases the electrochemical performance [36]. The values of contact angle are 34, 33, 31 and 31° for $x=0.02$, 0.05, 0.07 and 0.1, respectively. The results are in agreement with the FESEM images, which by adding Zn to $x=0.02$, initially increases the porosity at the film surface, but with increasing Zn concentration, the porosity of the films decreases. According

to the Wenzel equation, the films hydrophilic behavior was expected to increase with increasing roughness, but the films hydrophilicity decreased. This shows that the surface wettability behavior of our samples follows the Casey and Baxter model.

3.5 Optical properties

The optical properties of $Zn_x(Sb_2S_3)_{1-x}$ films measured with UV–Visible spectrometer. Optical transmission spectra of the films in the wavelength region of 200–900 nm are exhibited in Fig. 6. As expected, antimony sulfide films have low optical transparency. In the transmission spectrum of thin films, we can observe that by adding Zn impurities the fundamental absorption edge was shifted towards higher wavelengths. But with the increase of Zn concentration, the absorption edge of the film shifts again to shorter wavelengths, indicating a change in the band gap of the films. The shift of the absorption edge to shorter wavelengths can be attributed to the decrease in crystallites size. The decrease of the semiconductor crystallite size should be accompanied with a slight shift of the absorption band to higher frequency owing to the quantum confinement effect [37]. This behavior of the absorption edge corresponds to the results in the FESEM images and the strain changes in XRD analysis.

Puma software was used to find refractive index, extinction coefficient and film thickness. The results show that the thickness of the thin films produced is in the range 300 to 350 nm. The variations of refractive index and extinction coefficient with the wavelength for all the films are exhibited in Fig. 7. Among the all samples, the sample with x value of 0.02 has the highest refractive index. The

Fig. 5 The water contact angle for the $Zn_x(Sb_2S_3)_{1-x}$ thin films; **a** $x = 0.00$, **b** $x = 0.02$, **c** $x = 0.05$, **d** $x = 0.07$, **e** $x = 0.1$
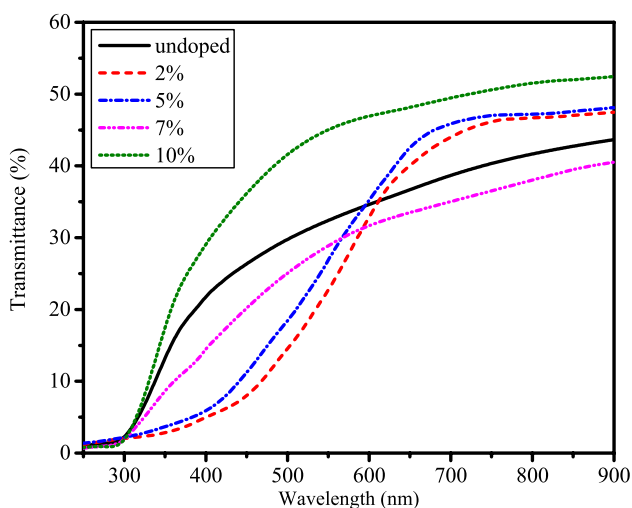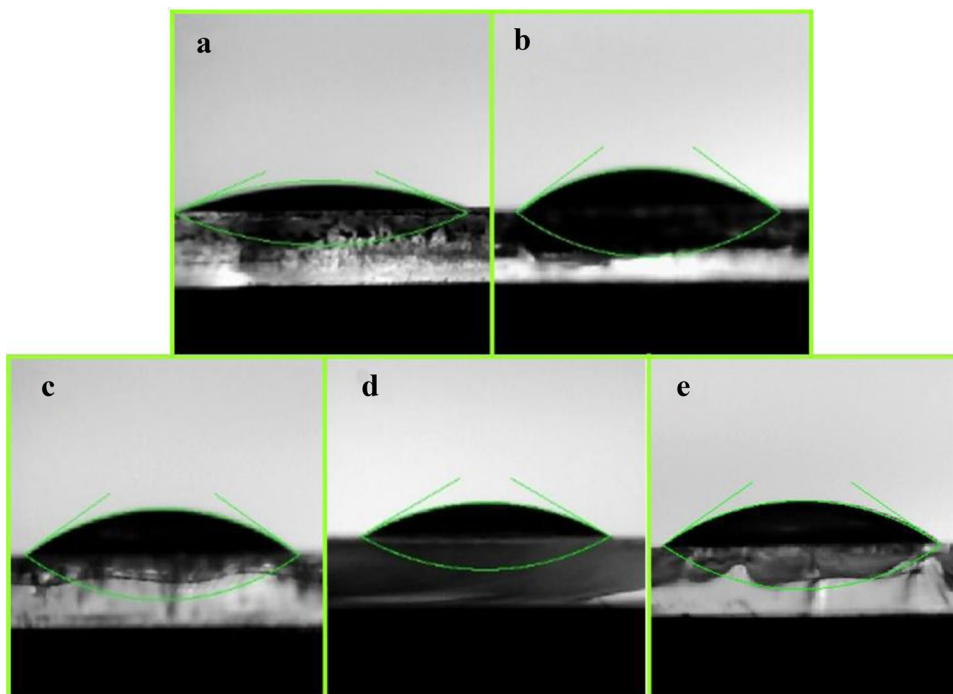

Fig. 6 Transmittance spectra of $Zn_x(Sb_2S_3)_{1-x}$ thin films

refractive index for all concentrations decreases at higher wavelengths. Changes in refractive index and extinction coefficient can be due to grains density and surface roughness of the films. To calculate the amount of direct optical band gap, the Tauc relation was used [38]:

$$(\alpha h\nu)^{\frac{1}{n}} = B(h\nu - E_g) \tag{5}$$

where $h\nu$ is the photon energy, B is the coefficient constant and n can be 1/2 and 2 for direct and indirect transition,

respectively, and α is also the absorption coefficient which can be calculated using the following equation [39]:

$$\alpha = -\frac{1}{d} \ln x \tag{6}$$

where d is the film thickness and x can be obtained from the following equation [39]:

$$x = \frac{(n-1)^3 (n + s^2) T}{16n^2 s} \tag{7}$$

where n is the refractive index of the film, s is the refractive index of the substrate and T is the transmittance of the film. The variations curve $(\alpha h\nu)^2$ whit $h\nu$ for $Zn_x(Sb_2S_3)_{1-x}$ thin films is shown in Fig. 8. As shown in figure, Zn doping reduced the band gap. Zn atoms form an acceptor alignment near edge of conduction band, resulting in a decrease in band gap. Sediment of sulfide around metallic ions creates local states and tracks near edge of conduction band leading to a decrease in band gap as well [26]. As the Zn concentration in the films increases, the band gap increases. This increase is due to the decrease in the number of surface particles due to the addition of Zn, which results in the formation of a more homogeneous film. This may also be due to new nucleation sites due to Zn dopant. Similar results were observed for the Sb_2S_3 band gap with Fe dopant [15]. Theoretically, the magnitude of band gap shift due to doping rate is specified by two opposite effects, namely band gap narrowing (BGN) and the band gap widening (BGW). The band gap widening is generally explained by Burstein–Moss effect where by the
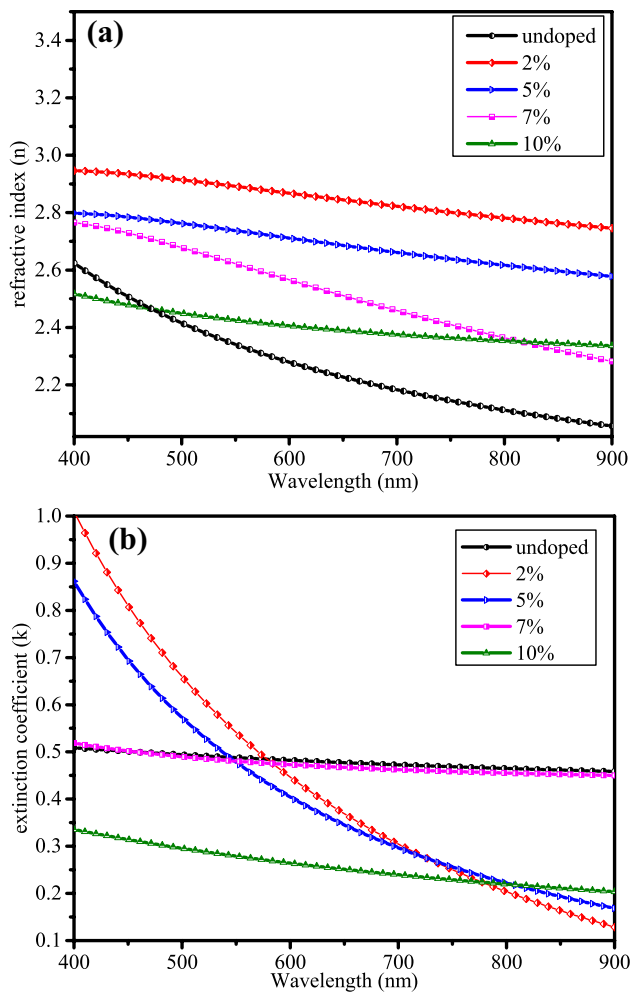
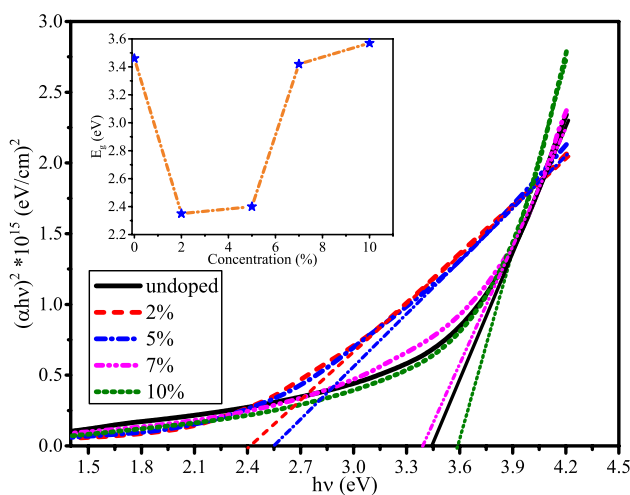**Fig.7** Refractive index and extinction coefficient with the wavelength of $Zn_x(Sb_2S_3)_{1-x}$ thin films

conduction band becomes filled at high doping concentration and the lowest energy states in the conduction band are clogged [40]. The values of band gap are 3.46, 2.35, 2.40, 3.42 and 3.57 eV for $x = 0.00$, 0.02, 0.05, 0.07 and 0.1, respectively.

3.6 Photoluminescence study

Figure 9 shows the photoluminescence emission spectra of zinc-doped Sb_2S_3 thin films taken at room temperature with an excitation wavelength of 280 nm. It is known that the main emission band is emitted at 392 nm (3.17 eV) and 417 nm (2.98 eV). Ultraviolet emission band with two peaks at wavelengths 392 and 417 nm is due to the recombination of excited state electrons [41]. The next peak is about 480 nm, which this blue emission can be attributed to the state of vacancy or defects in materials [33]. The peak at about 570 nm indicates green emission due to sulfur depletion or surface defects [42]. The last peak at 715 nm can be related to the red emission due to the centers-centered on the band structure [33]. With the addition of Zn dopant, the emission intensity of the peaks increases. However, as the Zn concentration increases, the intensity of the peaks decreases, which may be due to a decrease in the cavity in Sb_2S_3 and a decrease in the recombination rate [43].

4 Conclusions

The $Zn_x(Sb_2S_3)_{1-x}$ thin films were prepared by sol–gel dip-coating method. The value of zinc had noticeable effect on structural, morphological and optical properties of the samples. XRD patterns of samples show the formation of
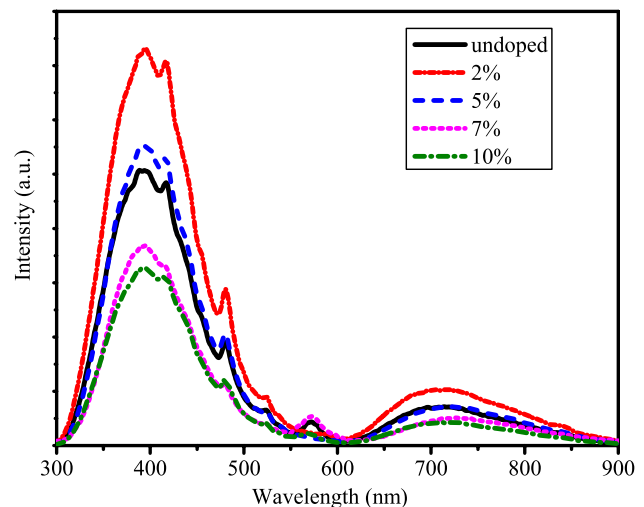

Fig.8 Plot of $(\alpha h\nu)^2$ vs. energy of $Zn_x(Sb_2S_3)_{1-x}$ thin films; **a** $x = 0.00$, **b** $x = 0.02$, **c** $x = 0.05$, **d** $x = 0.07$, **e** $x = 0.1$

Fig.9 Photoluminescence emission spectra of zinc-doped Sb_2S_3 thin films

orthorhombic phases. All samples have a polycrystalline structure and the intensity of the peaks decreases with increasing zinc dopant. FESEM images reveal reduction of grain size with increase in Zn content. The grain size in the prepared sample is about 30 nm. The hydrophilicity of surface was decreases by increasing zinc. Antimony sulfide thin films have low optical transmittance, indicating a high absorption of the films. By doping Zn the fundamental absorption edge was shifted towards higher wavelengths. With the increase of Zn concentration, the absorption edge of the films shifted again to shorter wavelengths. Upon Zn concentration, the optical band gap of the films was found to decrease from 3.46 to 2.37 eV. As the Zn concentration increases, the band gap increases, which may be due to the decrease in the grain size of the films. PL spectra analysis indicated that the main emission intensity of the peaks increases with the addition of Zn dopant. However, with increasing the doping concentration, the intensity of the peaks decreases, indicating a decrease in the recombination rate.

References

1. A.N. Kulkarni, M.R. Prasad, R.V. Ingle, H.M. Pathan, G.E. Eldesoky, M. Naushad, R.S. Patil, Opt. Mater. **46**, 536–541 (2015)
2. G. Murtaza, M. Akhtar, M.A. Malik, P. O'Brien, N. Revaprasadu, Mater. Sci. Semicond. Process. **40**, 643–649 (2015)
3. C.G. Anderson, Chem. Erde. **72**, 3–8 (2012)
4. S. Sundar, J. Chakravarty, Int. J. Environ. Res. Public Health. **7**, 4267–4277 (2010)
5. C. Lan, G. Liang, H. Lan, H. Peng, D. Su, D. Zhang, H. Sun, J. Luo, P. Fan, Phys. Status Solidi RRL **12**, 18–25 (2018)
6. M.Y. Versavel, J.A. Haber, Thin Solid Films **515**, 7171–7176 (2007)
7. V. Vinayakumar, C.O. Hernández, S. Shaji, D.A. Avellaneda, J.A. Martinez, B. Krishnan, Mater. Sci. Semicond. Process. **80**, 9–17 (2018)
8. J. Rodriguez-Castro, M.F. Mahon, K.C. Molloy, Chem. Vap. Depos. **12**, 601–607 (2006)
9. N. Ali, A. Hussain, R. Ahmed, W.W. Shamsuri, N.M. Abdel-Salam, R. Khenata, Appl. Phys. A. **123**, 282 (2017)
10. R.A. Garcia, C.M. Avendaño, M. Pal, F.P. Delgado, N.R. Mathews, Mater. Sci. Semicond. Process. **44**, 91–100 (2016)
11. N. Ali, A. Hussain, R. Ahmed, W.W. Shamsuri, A. Shaari, N. Ahmad, S.M. Abbas, Appl. Phys. A. **122**, 23 (2016)
12. E.K. Gil, S.J. Lee, S.J. Sung, K.Y. Cho, D.H. Kim, J. Nanosci. Nanotechnol. **16**, 10763–10766 (2016)
13. P.A. Nwofe, P.E. Agbo, C.O. Ozibo, Chalcogenide Lett. **13**, 10 (2016)
14. R. Tang, X. Wang, C. Jiang, S. Li, W. Liu, H. Ju, S. Yang, C. Zhu, T. Chen, A.C.S. Appl, Mater. Interfaces **10**, 30314–30321 (2018)
15. Z.U. Abdin, M.H. Alnasir, M.Y. Khan, M. Sajjad, M.T. Qureshi, A. Ullah, A. Zeb, Chalcogenide Lett. **16**, 1 (2019)
16. A. Alemi, Y. Hanifehpour, S.W. Joo, J. Nanomater. **20**, 46 (2011)
17. M.I. Medina-Montes, Z. Montiel-González, F. Paraguay-Delgado, N.R. Mathews, X. Mathew, J. Mater. Sci. Mater. Electron. **27**, 9710–9719 (2016)
18. S. Shaji, L.V. Garcia, S.L. Loredo, B. Krishnan, J.A. Martinez, T.D. Roy, D.A. Avellaneda, Appl. Surf. Sci. **393**, 369–376 (2017)
19. A.K. Zak, W.A. Majid, M.E. Abrishami, R. Yousefi, Solid State Sci. **13**, 251–256 (2011)
20. R.A. Young, *The Rietveld method*, 2nd edn. (Oxford University Press, New York, 1995), pp. 1–38
21. M. Trivedi, G. Nayak, S. Patil, R.M. Tallapragada, O. Latiyal, Ind. Eng. Manag. **4**, 165 (2015)
22. L. Dashairya, M. Sharma, S. Basu, P. Saha, J. Alloys Compd. **735**, 234–245 (2018)
23. S. Subramanian, D.P. Padiyan, Phys. B **405**, 925–931 (2010)
24. W. Hou, H. Guo, J. Zhang, J. Xu, L. Liu, Z. Zhang, J. Yang, B. Liang, H. Zhang, Mater. Lett. **216**, 73–76 (2018)
25. N.S. Tezel, F.M. Tezel, İ.A. Kariper, Appl. Phys. A. **125**, 198 (2019)
26. H. Behzad, F.E. Ghodsi, J Mater Sci: Mater. Electron. **27**, 6096–6107 (2016)
27. C.J. Diliegros-Godines, J.S. Cruz, N.R. Mathews, M. Pal, J. Mater. Sci. **53**, 11562–11573 (2018)
28. Z. Bazhan, F.E. Ghodsi, J. Mazloom, Surf. Coat. Technol. **309**, 554–562 (2017)
29. H.C. Barshilia, A. Chaudhary, P. Kumar, N.T. Manikandanath, Nanomaterials. **2**, 65–78 (2012)
30. S. Salari, F.E. Ghodsi, J. Mater. Sci. **53**, 11986–12004 (2018)
31. B. Yan, J. Tao, C. Pang, Z. Zheng, Z. Shen, C.H.A. Huan, T. Yu, Langmuir **24**, 10569–10571 (2008)
32. J. Lü, K. Huang, X. Chen, J. Zhu, F. Meng, X. Song, Z. Sun, Appl. Surf. Sci. **256**, 4720–4723 (2010)
33. A.N. Kulkarni, S.A. Arote, H.M. Pathan, R.S. Patil, Bull. Mater. Sci. **38**, 493–498 (2015)
34. S. Yao, J. Cui, J.Q. Huang, Z. Lu, Y. Deng, W.G. Chong, J. Wu, M. Ihsan Ul Haq, F. Ciucci, J.K. Kim, Adv. Energy Mater. **8**, 1800710 (2018)
35. X. Zhong, H. Zhao, H. Yang, Y. Liu, G. Yan, R. Chen, Appl. Surf. Sci. **289**, 425–429 (2014)
36. S.S. Karade, K. Banerjee, S. Majumder, B.R. Sankapal, Int. J. Hydrog. energy. **41**, 21278–21285 (2016)
37. M. Liu, Q. Zhan, W. Li, R. Li, Q. He, Y. Wang, J. Alloys Compd. **792**, 1000–1007 (2019)
38. J. Tauc, *Optical properties of solids*, 1st edn. (North-Holland, Amsterdam, 1972), pp. 277–313
39. Z. Bazhan, F.E. Ghodsi, J. Mazloom, Philos. Mag. **96**, 2953–2968 (2016)
40. A.A. Ziabari, S.M. Rozati, Phys. B **407**, 4512–4517 (2012)
41. W. Tao, J. Chang, D. Wu, Z. Gao, X. Duan, F. Xu, K. Jiang, Mater. Res. Bull. **48**, 538–543 (2013)
42. W.Z. Tawfik, A.A. Farghali, A. Moneim, N.G. Imam, S.I. El-Dek, Nanotechnology. **29**, 215709 (2018)
43. Q. Peng, J. Jie, C. Xie, L. Wang, X. Zhang, D. Wu, Y. Yu, C. Wu, Z. Wang, P. Jiang, Appl. Phys. Lett. **98**, 117–123 (2011)